

# Dynamic Analysis of Geogrid-Reinforced Pavement under Area Load Configuration: A Numerical and Field-Based Study

Aanchal Tiwari\*, Padma Bahadur Shahi, Rajan Suwal, Ram Chandra Tiwari

Department of Civil Engineering, Pulchowk Campus, Institute of engineering, Tribhuvan University, Lalitpur, 44600, Nepal

---

## Abstract

This study examines the stress-strain behavior of flexible pavements reinforced with geogrids, specifically focusing on the mid-thickness of the base layer where reinforcement is applied. The issue addressed is the structural and surface distresses in flexible pavements, worsened by improper load distribution. The aim is to evaluate the effectiveness of geogrid reinforcement in reducing vertical deformation and improving overall pavement performance under varying load and drainage conditions. The scope of the study includes a comparative analysis of unreinforced and geogrid-reinforced pavement sections, using two vehicle types (TATA Truck Tipper SK 1613 and Ford Ranger Pickup) and speed 15 km/h, modeled under both constant and accelerated conditions. Field instrumentation, including earth pressure cells, strain gauges, and moisture sensors, was placed at two sections 100 meters apart on the Arughat-Okhale Road section of the Mid-Hill Road Project. A 3D Finite Element Modeling (FEM) analysis using PLAXIS was performed, validated with field-measured data. The analysis focused on compressive and tensile stress and strain at the subgrade and base layers, including comparisons between drained and undrained subgrade conditions. Results show that geogrid reinforcement reduces vertical deformation, with higher geogrid stiffness further improving pavement performance. Modeling the subgrade as undrained proved suitable for accurately capturing stress redistribution in regions with significant moisture fluctuation, and these results aligned with field observation data. This research highlights the role of geotextiles and geogrids as composite materials in pavement systems, demonstrating their combined impact on stress distribution, reinforcement efficiency, and performance. The findings contribute to the understanding of geogrid technology in mitigating structural and surface distresses in flexible pavements.

*Keywords:* Geogrid Reinforcement; Field Instrumentation and monitoring; Stress-Strain Analysis; vehicle load configuration; Pavement performance.

---

## 1. Introduction

The Conventional pavements, consisting of subgrade, sub-base, and base layers, are designed primarily for compressive strength but are prone to tension-related failures such as cracking and rutting. This inherent weakness in tension makes pavements susceptible to degradation, particularly in regions with weak subgrade soils. Over the years, various methods have been proposed to improve pavement performance, and one of the most effective solutions is the reinforcement of pavements with geosynthetics, such as geogrids. These materials enhance tensile strength, provide lateral restraint, and reduce pavement deformation, significantly improving overall durability and performance (FPDG, 2014; IRC: 37, 2018). Geogrids function by establishing an interlock mechanism with aggregates, distributing applied loads more effectively and reducing vertical deformation (Ahirwar & Mandal, 2017; Bhandari & Han, 2010; Wang et al., 2014). This reinforcement method has shown promising results in stabilizing pavements on weak subgrade soils, mitigating issues such as fatigue cracking and rutting, which arise from tensile strain and vertical subgrade strain, respectively (Bhandari & Sharbaf, 2019; Tang et al., 2016). Additionally, geogrids help in preventing material mixing between pavement layers, enhance subsurface drainage, and reduce reflective cracking, offering both economic and environmental benefits (Zornberg, 2017; Wu et al., 2015).

Despite the advantages of geogrid reinforcement, current pavement design methods predominantly rely on static loading assumptions, which fail to account for the dynamic effects of moving traffic. This shortcoming results in inaccurate strain predictions, potentially leading to less efficient and overly conservative pavement designs (Wu et al., 2020; Nader & Sharbaf, 2016). Traditional models are based on the assumption of static, uniform loads;

---

\* E-mail address: 079mstre001.aanchal@pcampus.edu.np

however, the actual behavior of pavements under traffic conditions involves dynamic loading, which causes significant strain variations and affects pavement longevity. By not considering the dynamic loading effects, traditional design methods cannot accurately predict pavement performance in real-world conditions (Liu et al., 2020; Wang et al., 2015). The need to incorporate dynamic traffic loading effects into pavement design models is critical for improving the accuracy of strain predictions and ensuring more durable pavements in areas with fluctuating traffic volumes and load conditions (Zhang et al., 2016; Sharma et al., 2021).

Geogrids offer a practical and cost-effective alternative to traditional mechanical stabilization methods or additive treatments for improving weak subgrade soils, which can be both expensive and challenging to implement (Bajracharya & Sharma, 2015; Zornberg, 2017). By enhancing load distribution and reducing pavement deformation, geogrids perform similarly to steel reinforcement in concrete, but without the high costs and complexities associated with traditional reinforcement techniques (Nik Daud et al., 2019). This research seeks to evaluate the stress and strain variations in pavements reinforced with geogrids under both static and dynamic loading conditions. Through a combination of physical and numerical modeling, the study aims to improve the accuracy of numerical models for reinforced pavement design by comparing these models' predictions against real-world data collected from physical models equipped with sensors, such as earth pressure gauges, strain gauges, and moisture sensors (Pazhani et al., 2016; Roy et al., 2018).

The primary aim of this study is to assess the effectiveness of geogrid reinforcement in enhancing pavement performance, particularly in reducing deformation, controlling cracking, and improving load distribution under dynamic loading scenarios. The research will focus on low-volume roads and pavements constructed on weak subgrade soils, where conventional pavement design approaches may not provide sufficient strength or stability (Siddique et al., 2020; Sharma et al., 2016). Low-volume roads in regions with weak subgrades are particularly prone to issues such as fatigue cracking and rutting, which are exacerbated by dynamic traffic loads (Bhandari & Han, 2010; Bhandari & Sharbaf, 2019). The study will address the gap in the literature concerning the dynamic effects of traffic loading and its role in pavement performance, particularly for regions that experience varying load conditions (Liu et al., 2020).

Furthermore, the study will provide a framework for validating numerical models used for analyzing geosynthetic-reinforced pavements, focusing on the importance of including dynamic traffic loading effects in these models (Mandal et al., 2017). While physical models equipped with various sensors can provide essential empirical data, they are often expensive and time-consuming to implement (Wu et al., 2020). For large-scale analysis, numerical models offer a more cost-effective and efficient alternative for evaluating pavement performance across different traffic and environmental conditions. By simulating different traffic and environmental conditions, this research will provide valuable insights into the role of geosynthetics in improving pavement durability, particularly in regions prone to extreme weather or high rainfall (Thakur et al., 2017; Pazhani et al., 2016).

Ultimately, the findings of this study will help refine existing pavement design methods by incorporating the dynamic effects of traffic loads and better representing the real-world performance of geogrid-reinforced pavements (Zornberg et al., 2015; Sharma et al., 2021). The outcomes will provide guidelines for optimizing pavement reinforcement strategies, particularly for regions with challenging subgrade conditions, complex traffic patterns, and extreme environmental factors (Khatri et al., 2019; Roy et al., 2018). This research aims to contribute to the development of more resilient, cost-effective, and sustainable pavement systems, offering a better understanding of how geosynthetics can enhance pavement design and long-term performance.

## **2. Study Area**

The selected study area, located on the Arughat-Okhale road section of the Mid-Hill Road Project in Gorkha, Nepal, is part of a national infrastructure initiative currently under construction, serving as a national pride project for Nepal. The timing of this project provides a unique opportunity to observe and assess pavement performance from the early stages of construction to the road use phase. Sensors, including earth pressure gauges, strain gauges, and moisture sensors, compatible with a geodynamic data logger, are installed at the mid-thickness of the base layer, which was specifically chosen for geogrid placement. These sensors are capable of capturing both short and long-term data, enabling a comprehensive evaluation of the impact of the 40/40Q Tensar polypropylene geogrid on stress distribution and pavement performance. Monitoring the pavement's behavior and assessing the effect of geogrid reinforcement allows for a detailed understanding of how such materials contribute to road longevity, particularly under real-world traffic conditions. Additionally, historical issues with structural deficiencies and surface distresses in other sections of the Mid-Hill Road have highlighted the need for effective solutions to improve pavement performance. The study area as shown in Figure 1 includes location map along with both

unreinforced and geogrid-reinforced pavement sections, with the unreinforced section located at CH 1+700 (28° 2'22.51"N, 84°48'29.03"E) and the geogrid-reinforced section at CH 1+800 (28° 2'20.48"N, 84°48'27.42"E). The Budhigandaki Bridge at CH 0+000 serves as the reference point for these locations.

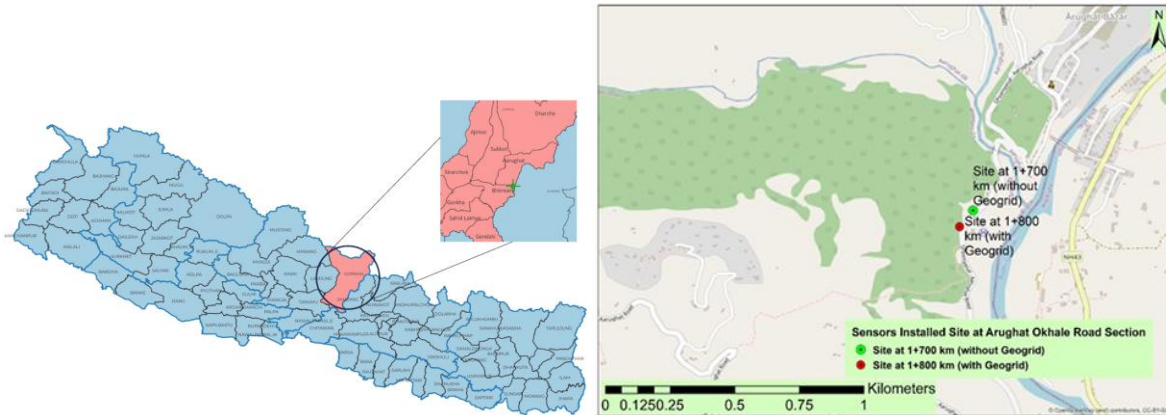


Figure 1. Study area showing test location: Location map showing District map (Left Figure). The test sites on the Aarughat-Okhale Road Section, Mid-Hill Road Project, Gorkha. The unreinforced section is at CH 1+700 (28° 2'22.51"N, 84°48'29.03"E) and the geogrid-reinforced section at CH 1+800 (28° 2'20.48"N, 84°48'27.42"E), with the Budhigandaki Bridge at CH 0+000 as the reference point (Right Figure)

### 3. Material and Method

#### 3.1 Geometrical Model

The geometrical model was developed based on the design and construction details of the Mid-Hill Road Project (Figure 2). For the base course thickness, the model reflects the actual conditions of the Aarughat-Okhale road section, where the base course is 20 cm thick, paired with a 20 cm subbase layer and a 3 cm thick Double Bituminous Surface Treatment (DBST). The model was adjusted to accurately represent the site conditions, with vehicle-related parameters and soil material properties treated as variables to evaluate their impact on pavement performance.

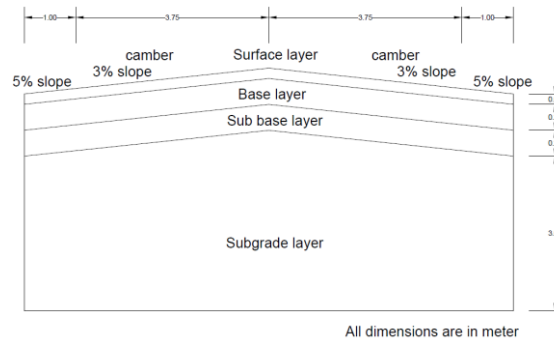


Figure 2. Geometrical model of the Aarughat-Okhale Road Section, Mid-Hill Road Project, Gorkha. The unreinforced section is at CH 1+700 (28° 2'22.51"N, 84°48'29.03"E) and the geogrid-reinforced section at CH 1+800 (28° 2'20.48"N, 84°48'27.42"E), with the Budhigandaki Bridge at CH 0+000 as the reference point

#### 3.2 Material Model

The thickness and properties of the subgrade, sub-base, and base layers were determined through a combination of field and laboratory tests. Laboratory CBR values of subgrade soils were explored and compared with field Dynamic Cone Penetrometer Tests (DCPT), which assessed the subgrade's strength, while Triaxial testing measured the subgrade modulus, crucial for accurately modeling the pavement's behavior under load. Data from the Mid-Hill Road Project were analyzed, revealing that the crushed stone base CBR at 98% maximum dry density was 90.44% at CH 1+200, 90.97% at CH 2+300, 87.58% at CH 8+700, and 81% at CH 12+200. Similarly, the CBR of subbase material at CH 10+000 was 35% (DPR, Midhill project report, 2011). The subgrade modulus,

determined from Triaxial testing, was 13099.3 kN/m<sup>2</sup>, with a surface modulus of 35.887 MPa, according to IRC:37 (2018).

The field DCPT test is conducted during the preparation of the subgrade, subbase, and base course, as outlined in Table 1. The Dynamic Cone Penetration Index (DCPI), expressed as penetration per blow, is used to calculate the corresponding CBR% based on the correlation provided by the U.S. Army Engineer Waterways Experiment Station (1992).

$$LOG(CBR) = 2.46 - 1.12 LOG(DPI) \tag{1}$$

The results of the Dynamic Cone Penetration Test (DCPT) at various chainages are presented in Table 1.

Table 1. Dynamic Cone Penetration Test (DCPT) at various chainages

Pavement Layer	CBR%	CBR% suggested	Reference
Subgrade	4.93		1+700CH
	5.27	5.0	1+750CH
	5.08		1+800CH
Subbase	34.55	35.0	1+700CH
	35.40		1+800CH
Base	85.44	85.0	1+700CH
	85.54		1+800CH

Table 2 provides detailed material properties for each pavement layer incorporated into the numerical model.

Table 2. Material properties of pavement layers used in numerical modelling

Item	Description
Identification	Subgrade
Material model/Drainage type	Linear elastic/Undrained/Drained
Unsaturated/Sat. unit weight, $\gamma_{unsat}$ (kN/m <sup>3</sup> )	18/20
Poisson's ratio	0.35
Identification	Granular layer
Material model/Drainage type	Linear elastic/Drained
Unsaturated/Sat. unit weight, $\gamma_{unsat}$ (kN/m <sup>3</sup> )	19/21
Resilient modulus, E (MPa)	$E = 0.2 * (h)^{0.45} * MR_{support}$ (FPDG, 2014) Where, h = thickness of granular layer in mm $MR_{support}$ = (effective) resilient modulus of the supporting layer (MPa)
Poisson's ratio	0.35
Identification	Surface layer (GBST)
Material model/Drainage type	Linear elastic/Non-porous
Unsaturated unit weight, $\gamma_{unsat}$ (kN/m <sup>3</sup> )	20
Resilient modulus, E (MPa)	2000 (FPDG, 2014)
Poisson's ratio	0.35

For this study, a biaxial 40/40Q Tensar geogrid was chosen due to its effectiveness in flexible pavement base courses, where multidirectional stresses are common. With a tensile strength of 16 kN/m at 2% strain, this geogrid is well-suited for the expected low to medium traffic volume on the road section, providing essential reinforcement to prevent structural failure under loading. The biaxial configuration is particularly beneficial for reinforcing the base layer, where both horizontal and vertical forces must be efficiently distributed. The selected aperture size of 31 mm x 31 mm allows optimal reinforcement, enabling the base course material to interlock with the geogrid, facilitating effective load transfer, and providing strong support for the pavement structure.

The inclusion of the biaxial 40/40Q Tensar geogrid helps reduce both compressive and tensile stress-strain at the top of the subgrade and base layers. By improving load distribution across the base course, it minimizes surface distresses such as rutting and cracking, significantly enhancing the structural integrity and long-term performance of the pavement. While placing the geogrid at 100% of the base thickness (at the top of the base layer) is generally considered optimal, this configuration is not ideal for Double Bituminous Surface Treatment (DBST) layers, as different configurations may yield better results. The thin surface of DBST could interfere with sensor readings, so to ensure accurate data collection and sensor protection, sensors were installed at the mid-depth of the base course.

Field instrumentation, including sensors for stress, strain, and moisture content, was crucial for validating the simulation results. These measurements provided valuable real-world data on how the geogrid influences pavement performance under actual traffic and environmental conditions, enhancing the accuracy and relevance of the study. The base course, located between the subgrade and surface layer, was selected for both geogrid placement and sensor installation due to its central role in load distribution and stress-strain behavior. This layer is especially vulnerable to tensile stresses, making it a critical location for reinforcement to prevent structural failures such as cracks and rutting. Due to practical challenges with sensor placement in upper layers, such as beneath the DBST, the mid-depth of the base course was chosen for geogrid placement. This ensures effective tensile force distribution and reduces vertical strain at the top of the subgrade, mitigating stresses under dynamic loading. Furthermore, placing the geogrid at mid-depth protects it from direct exposure to wear while reinforcing the pavement structure, ensuring both effectiveness and durability. By reinforcing the mid-level of the base course, the study helps prevent deformation and cracking from repetitive traffic loads, extending the pavement’s service life.

The Tensar 40/40Q geogrid consists of polypropylene (PP) strands arranged in a regular grid pattern, with a strand diameter of 3 mm and an aperture size of 31 mm x 31 mm. The geogrid has 32 strands per meter in width, which results in a total cross-sectional area of  $2.26 \times 10^{-4} \text{ m}^2$ . For the woven polypropylene geotextile, which is commonly used for both separation and reinforcement, we consider a geotextile thickness of 0.5 mm (0.0005 m) and a width of 1 meter. This gives a geotextile cross-sectional area of  $5 \times 10^{-4} \text{ m}^2$ . The geotextile has varying tensile strengths of 40 kN/m, 80 kN/m, and 120 kN/m, and its stiffness is calculated based on its tensile strength and cross-sectional area. To calculate the total stiffness when both the geogrid and geotextile are placed together, we sum the stiffness values of the geogrid and geotextile. The geogrid has stiffness values of 800 kN/m, 1100 kN/m, and 1250 kN/m. If both geotextile and geogrid are employed as composite materials, the stiffness to be used in numerical modeling should follow the values provided in Table 3.

For geogrid material, the axial stiffness is the ratio of the axial force  $F$  per unit width and the axial strain ( $\Delta l/l$  where  $\Delta l$  is the elongation and  $l$  is the original length):

$$EA = F / (\Delta l / l) \tag{2}$$

For isotropic material Shear stiffness  $(GA) = EA/2$ . The Lab test data from Tensar bi-axial geogrid is given as:

Table 3. Calculation of equivalent geogrid stiffness for composite material

Geogrid Stiffness (k1) kN/m	Geotextile Stiffness (k2) kN/m	Geotextile Contribution (Delta_k) (kN/m)	Equivalent Geogrid Stiffness (kEq.) (kN/m)
800	40	39.48	839.48
800	80	78.96	878.96
800	120	118.44	918.44
1100	40	39.48	1139.48
1100	80	78.96	1178.96
1100	120	118.44	1218.44
1250	40	39.48	1289.48
1250	80	78.96	1328.96
1250	120	118.44	1368.44
1600	40	39.48	1639.48
1600	80	78.96	1678.96
1600	120	118.44	1728.44
3200	40	39.48	3239.48
3200	80	78.96	3287.96
3200	120	118.44	3328.44
5000	40	39.48	5039.48
5000	80	78.96	5078.96
5000	120	118.44	5118.44

### 3.3 Method

The Figure 3 outlines the methodology for validating numerical results, comparing geogrid-reinforced and unreinforced pavement sections. The study focuses on stress, strain, and structural integrity to assess the geogrid's impact on load distribution and deformation resistance, aiming to improve pavement stability, longevity, and resilience.

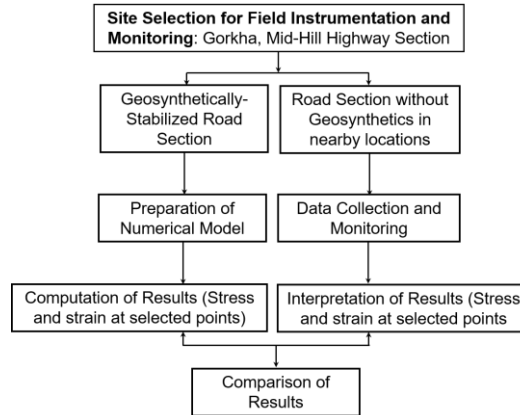


Figure 3. Methodology flowchart for numerical validation of pavement reinforcement effectiveness

In the dynamic modeling of the pavement system, the following parameters were considered: the Modulus of Elasticity for both the geogrid and pavement layers, Poisson’s Ratio to characterize the material's lateral strain response to vertical compression, and Vehicle Motion Parameters, including speed, acceleration, frequency, and amplitude of wheel motion, to replicate real-world dynamic loading conditions. The mesh generation used a relative element size of 0.5, with ten-node tetrahedral elements, ensuring a balanced approach to both model accuracy and computational efficiency. This mesh density was sufficient to capture the crucial interactions between the geogrid and the surrounding pavement layers.

Dynamic loading systems were used to simulate real-world traffic scenarios, capturing the pavement's response to both stationary and moving loads. Static loads, representing the weight of parked vehicles, were applied to analyze deformation and stress distribution at specific points in time. In contrast, dynamic loads replicated the fluctuating stresses generated by moving traffic, allowing for the assessment of how repetitive traffic cycles affect the pavement. Vehicle speeds of 15 km/h, along with accelerations of 1.0 m/s<sup>2</sup>, were considered to simulate varying traffic conditions, including both light and heavy vehicle movements. This dual approach enabled a comprehensive evaluation of the geogrid's performance under different loading scenarios.

The study primarily focused on the area load configuration, as it more accurately represents the tire contact area compared to the point and line load configurations. The 4-wheel Ford Ranger Pickup and the 6-wheel Tata Truck Tipper SK 1613 were used, with loads applied at each wheel. For the 4-wheel configuration, 20 kN per wheel (80 kN total) was applied. For the 6-wheel configuration, 40 kN per axle was applied, again resulting in a total of 80 kN. The area load distribution followed guidelines from the FPDG (2021) to accurately model the transfer of load from tires to pavement.

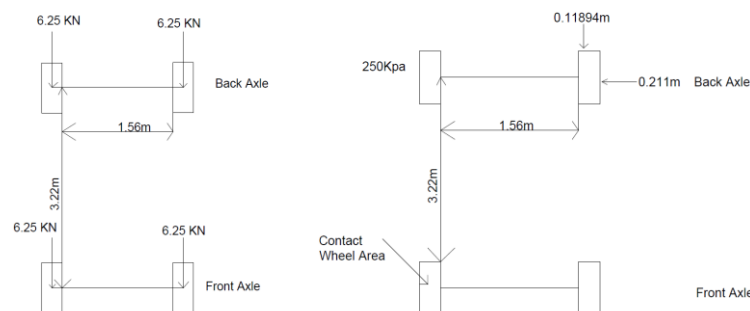


Figure 4. Standard axle load configuration of FORD RANGER PICKUP: Point load (Left Figure); Area load (Right Figure)

The time period of the wheel cycle (Tcycle, Sec. ), frequency of motion (f, Hz), angular velocity ( $\Omega$ , rad/sec), phase angle ( $\phi$ , degree), and dynamic time steps ( $\Delta t$ , Sec.) can be calculated using Equations (3) to (7), respectively.

$$T_{cycle} = P(\text{perimeter of wheel in m.})/v(\text{velocity in m/sec.}) \tag{3}$$

$$f = 1/T_{cycle} \text{ (Sec.)} \tag{4}$$

$$\Omega = 2 \pi f \text{ (rad/sec)} \tag{5}$$

$$\phi = \text{Wheel base (m)}/\text{Radius of curve (m)} \tag{6}$$

$$\Delta t = T_{cycle} \text{ (sec)}/\text{No. of time steps (No.)} \tag{7}$$

The dynamic parameters for harmonic motion of both constant and accelerated motions are shown in Table 4.

Table 4. Parameters for harmonic motion of vehicle for constant and accelerated motion

Vehicle speed (km/hr)	Speed (m/sec)	Base frequency (Hz)	Base amplitude (m)	Accelerated amplitude at a=0.5m/sec <sup>2</sup>	Accelerated amplitude at a=0.5m/sec <sup>2</sup>	Accelerated frequency at a=0.5m/sec <sup>2</sup>	Accelerated frequency at a=0.5m/sec <sup>2</sup>	Phase angle (Degrees)	Dynamic Time for time step 100 (Seconds)
TATA TRUCK TIPPER SK 1613									
5	1.39	0.42	0.525	0.552	0.578	0.44	0.46	0	0.0237
15	4.17	1.25	0.531	0.557	0.584	1.30	1.32	0	0.00794
FORD RANGER PICKUP									
5	1.39	0.42	0.528	0.524	0.522	0.44	0.46	0	0.02242
15	4.17	1.25	0.667	0.662	0.660	1.30	1.32	0	0.007535

This model is specifically configured to analyze the effect of geogrid reinforcement on load distribution and structural integrity, enabling a precise comparison between reinforced and unreinforced sections. The Geogrid used is a monolithic polypropylene 40/40 Q Secugrid Q (PP) from Naue GmbH & Co. KG, Germany. The polypropylene geogrid features a mass per unit area of 240 g/m<sup>2</sup>, designed to offer robust support for soil reinforcement. It provides a maximum tensile strength of  $\geq 40$  kN/m, with an elongation at normal strength of  $\leq 7\%$ , ensuring minimal stretching under standard loads. The tensile strength at specified elongation levels is as follows: 8 kN/m at 1% elongation, 16 kN/m at 2% elongation, and 32 kN/m at 3% elongation, which supports incremental strength for various applications. The geogrid’s aperture size measures approximately 31 x 31 mm, facilitating effective interlocking with aggregate materials. The roll dimensions are 4.75 meters in width and 100 meters in length, offering substantial coverage for large-scale installations. This research utilized a Geodynamic data logging system, specifically designed to monitor pavement performance under real-time vehicle loading conditions. This system, referred to as the Instrument GeoDynamic Monitoring Set, consists of various components that collaboratively capture essential data on stress, strain, and moisture within the pavement structure. Figure 5 illustrates the field instrumentation and monitoring setup: the use of sensors in the unreinforced road section (Left Figure) and the data monitoring setup (Right Figure), which includes strain gauges, earth pressure sensors, and moisture measurement devices.



Figure 5. Field instrumentation and monitoring (strain gauge, earth pressure, and moisture): Use of sensors in unreinforced road section (Left Figure); Data monitoring setup (Right Figure)

#### 4. Results and Discussion

The results of the analysis indicate that Geogrid reinforcement plays a crucial role in enhancing pavement performance under dynamic loading conditions. The numerical results under undrained conditions closely match field observation data, validating the inclusion of undrained modeling in the study. Figure 6 shows the deformed mesh of the pavement model for the TATA Truck Tipper. Figure 7 illustrates that Geogrid reinforcement significantly reduces earth pressure, preventing the concentration of high stresses that could otherwise damage the pavement. The effect of the Geogrid on stress distribution is further confirmed in Figure 8, where the total stress ( $\Sigma 1$ ) along the road width is more evenly distributed when Geogrid is present, indicating better load-bearing capacity and reduced risk of pavement failure. Similarly, Figure 9 shows that Geogrid reinforcement reduces strain concentrations, particularly in the longitudinal direction, highlighting its effectiveness in improving resistance to deformation under the truck's dynamic load. Figure 10 further confirms these findings, as it shows reduced displacements in the pavement, particularly in the transverse direction, with the Geogrid in place. These results suggest that Geogrid reinforcement prevents excessive movement of the pavement, thereby prolonging its lifespan.

For the lighter 4-wheeled Ford Ranger Pickup, Figure 11 presents a deformed mesh that reveals less overall stress compared to the TATA Truck. However, even in this case, Figure 12 shows that the absence of Geogrid reinforcement results in higher localized stresses, underscoring the importance of reinforcement for optimal load distribution. The reduction in stress with Geogrid reinforcement is further evident in Figure 13, where principal total stress is more evenly spread, and improving pavement performance. Finally, Figures 14 to 16 show that the strain and displacement in both longitudinal and transverse directions are significantly reduced with Geogrid reinforcement in the Ford Ranger model. The longitudinal direction exhibits a more considerable reduction in strain, demonstrating the effectiveness of Geogrid reinforcement in maintaining pavement stability under dynamic loads. Overall, these results demonstrate that Geogrid reinforcement consistently improves the structural performance of pavements, particularly in preventing high stress concentrations and reducing deformation, with more significant benefits observed for heavier vehicles.

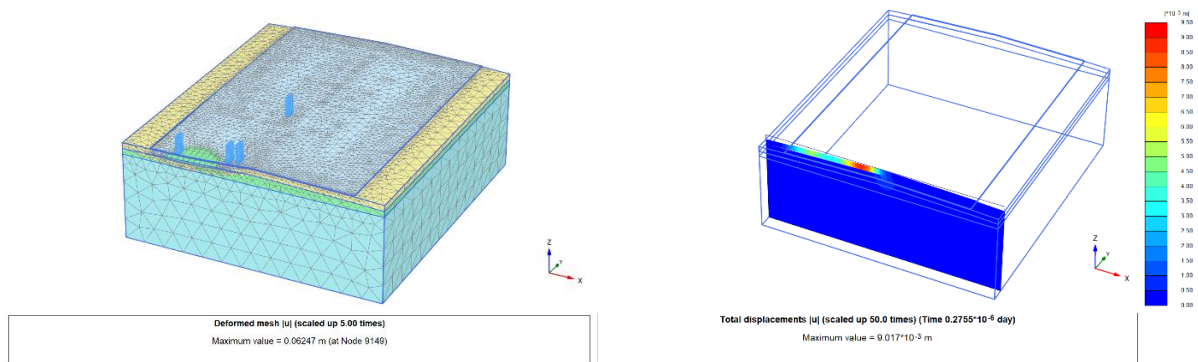


Figure 6. Deformed mesh of area load configuration pavement model in the Plaxis 3D domain and its vertical sectional view along the road width from the 6-wheeled TATA Truck Tipper SK 1613, traveling at a speed of 15 km/h with an accelerated motion of 1.0 m/s<sup>2</sup> on a undrained subgrade without Geogrid reinforcement of stiffness  $k = 800$  kN/m: Discretized model (Left figure); Sectional view (Right figure)

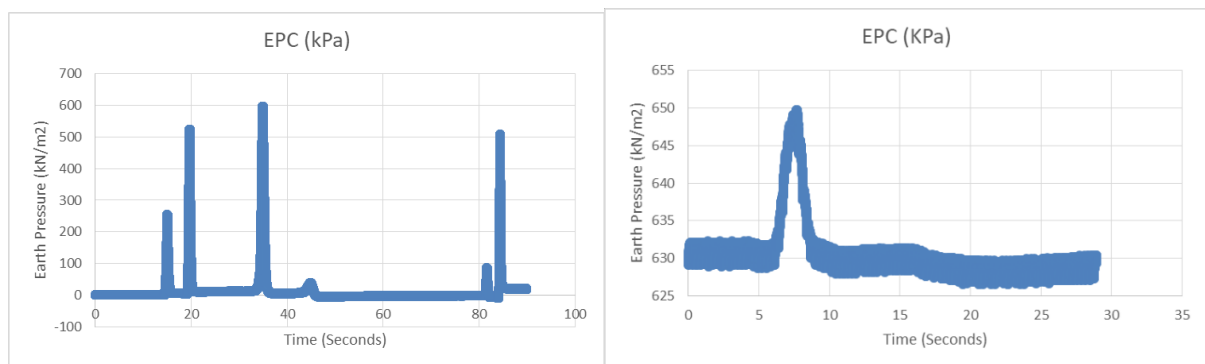


Figure 7. Field-measured Earth Pressure Distribution data from the 6-wheeled TATA Truck Tipper SK 1613, traveling at a speed of 15 km/h with an accelerated motion of 1.0 m/s<sup>2</sup>: Without Geogrid reinforcement (Left figure); With Geogrid reinforcement of stiffness  $k = 800$  kN/m (Right figure)

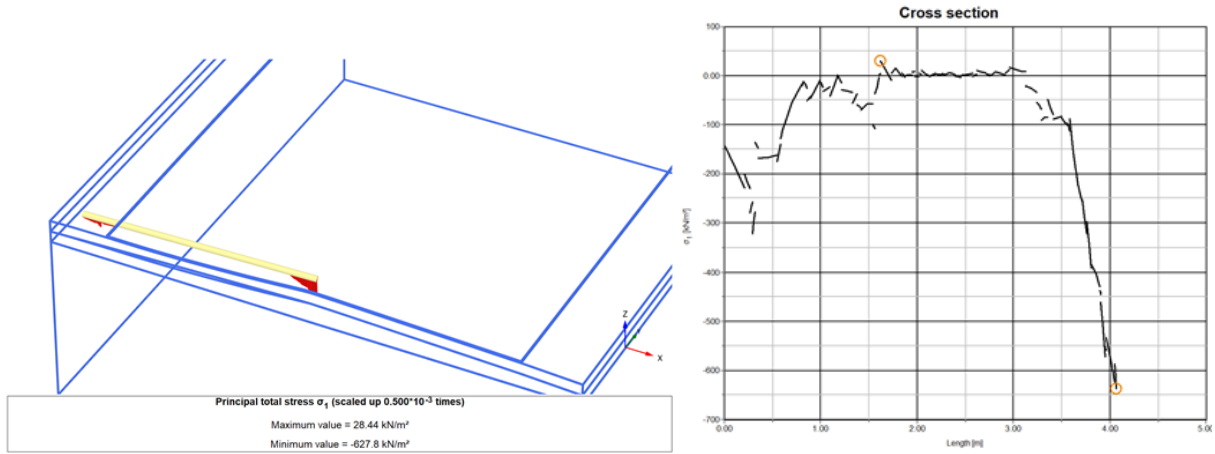


Figure 8. Numerically computed Total Stress (Sigma 1) along the width of the road at 0.5 m from the edge of the road under the 6-wheeled TATA Truck Tipper SK 1613, traveling at a speed of 15 km/h with Geogrid reinforcement of stiffness  $k = 800 \text{ kN/m}^2$  considering undrained subgrade: Total stress 'Sigma 1' diagram (Left figure); Total stress 'Sigma 1' plot (Right figure)

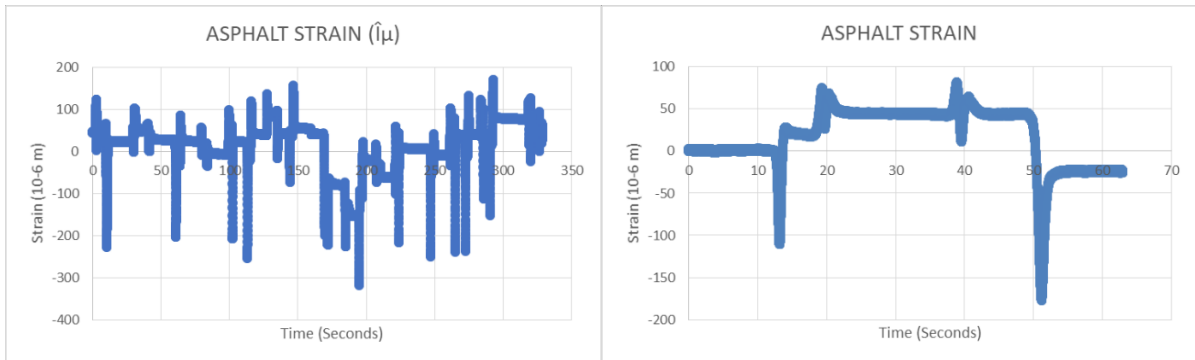


Figure 9. Field-measured strain distribution data from the 6-wheeled TATA Truck Tipper SK 1613, traveling at a speed of 15 km/h with an accelerated motion of  $1.0 \text{ m/s}^2$ , with Geogrid reinforcement of stiffness  $800 \text{ kN/m}$ : Longitudinal direction (along the wheel path) (Left figure); Transverse direction (across the width of the vehicle) (Right figure)

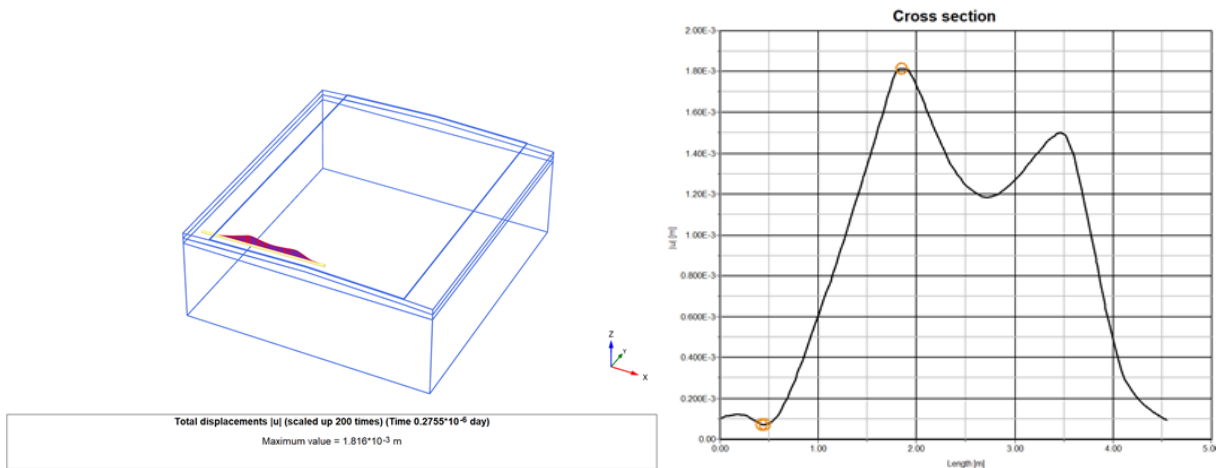


Figure 10. Numerically computed strain distribution data from the 6-wheeled TATA Truck Tipper SK 1613, traveling at a speed of 15 km/h with an accelerated motion of  $1.0 \text{ m/s}^2$ , with Geogrid reinforcement of stiffness  $800 \text{ kN/m}$  in the transverse direction (width of the vehicle) considering undrained subgrade: Total displacement diagram (Left figure); Total displacement plot (Right figure)

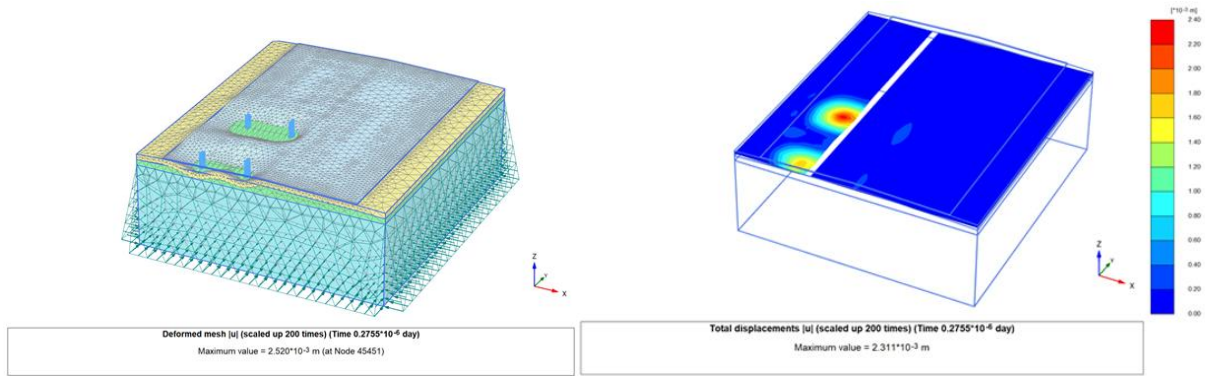


Figure 11. Deformed mesh of area load configuration of the pavement model in the Plaxis 3D domain and its horizontal sectional view from the 4-wheeled Ford Ranger Pickup, traveling at a speed of 15 km/h with an accelerated motion of 1.0 m/s<sup>2</sup> on an undrained subgrade without Geogrid reinforcement of stiffness  $k = 800$  kN/m: Deformed model (Left figure); Sectional view (Right figure)

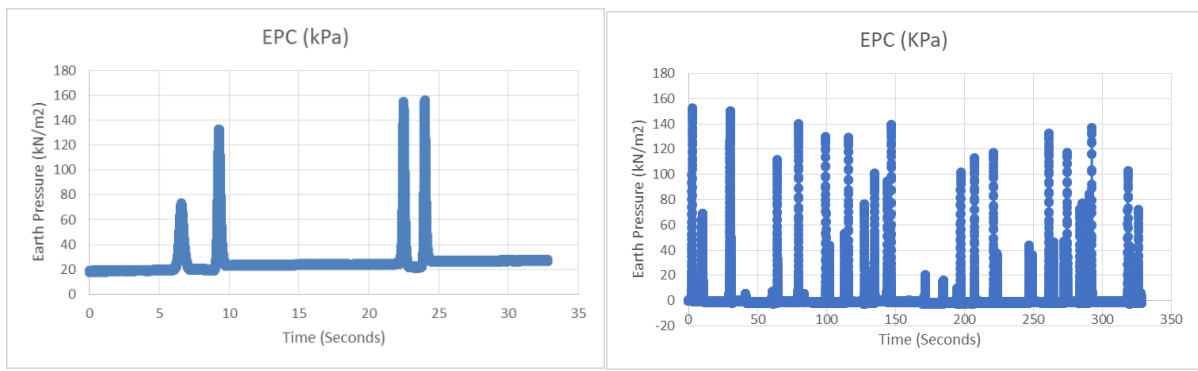


Figure 12. Field-measured Earth Pressure Distribution data from the 4-wheeled Ford Ranger Pickup, traveling at a speed of 15 km/h with an accelerated motion of 1.0 m/s<sup>2</sup>: Without Geogrid reinforcement (Left figure); With Geogrid reinforcement of stiffness 800 kN/m (Right figure)

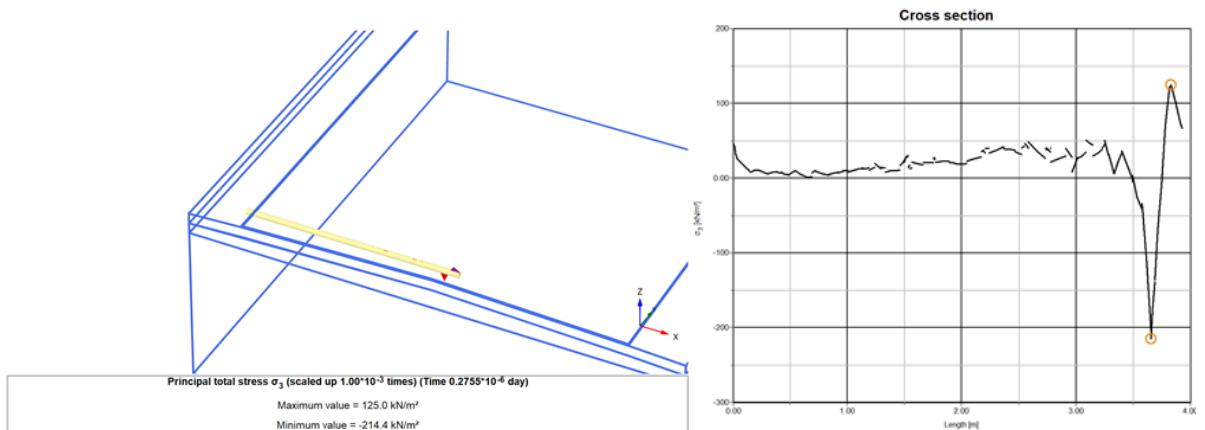


Figure 13. Numerically computed earth pressure distribution data from the 4-wheeled Ford Ranger Pickup, traveling at a speed of 15 km/h with an accelerated motion of 1.0 m/s<sup>2</sup> in the transverse direction (across the wheel width) under undrained subgrade conditions: Principal total stress diagram (Left figure); Principal total stress plot (Right figure)

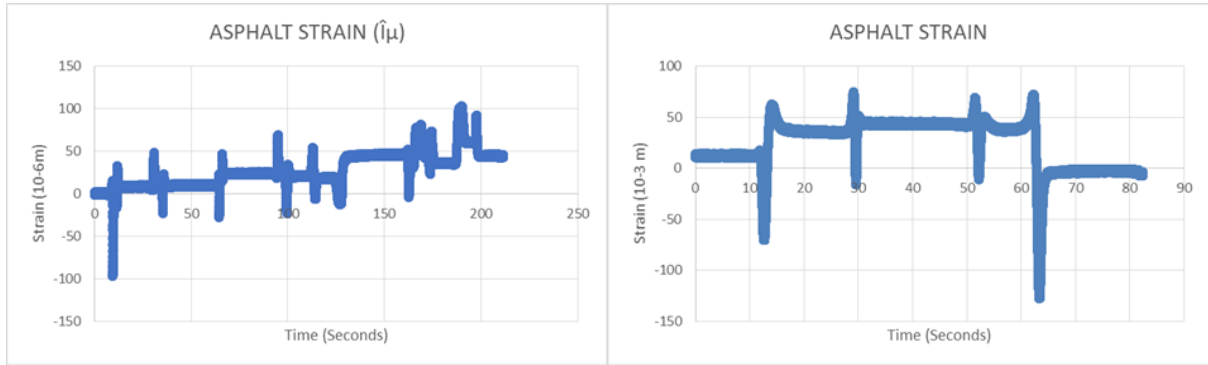


Figure 14. Field-measured strain distribution data from the 4-wheeled Ford Ranger Pickup, traveling at a speed of 15 km/h with an accelerated motion of 1.0 m/s<sup>2</sup> and Geogrid reinforcement of stiffness k = 800 kN/m: Longitudinal direction (along the wheel path) (Left figure); Transverse direction (across the width of the road) (Right figure)

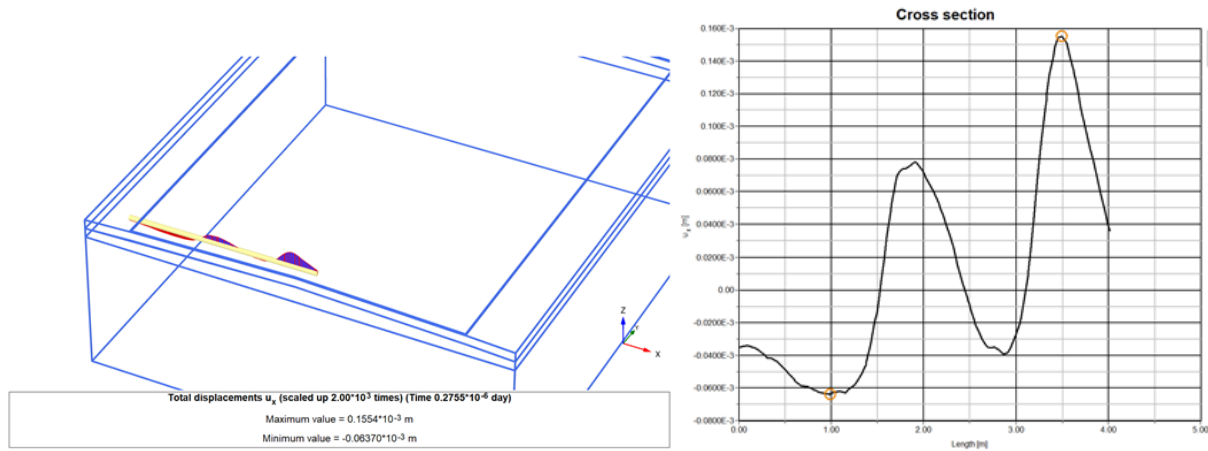


Figure 15. Numerically computed strain distribution data from the 4-wheeled Ford Ranger Pickup, traveling at a speed of 15 km/h with an accelerated motion of 1.0 m/s<sup>2</sup> and Geogrid reinforcement of stiffness k = 800 kN/m in the transverse direction (across the width of the road) considering undrained subgrade: Total displacement diagram (Left figure); Total displacement plot (Right figure)

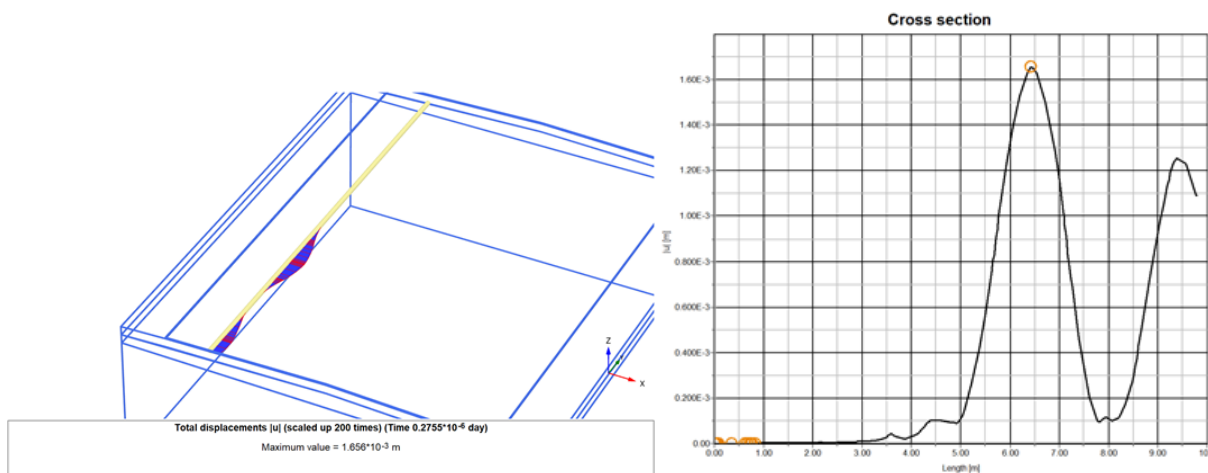


Figure 16. Numerically computed strain distribution data from the 4-wheeled Ford Ranger Pickup, traveling at a speed of 15 km/h with an accelerated motion of 1.0 m/s<sup>2</sup> and Geogrid reinforcement of stiffness k = 800 kN/m in the longitudinal direction (along the wheel path) considering undrained subgrade: Total displacement diagram (Left figure); Total displacement plot (Right figure)

In the analysis of the 6-wheel surface load with Geogrid reinforcement, the stress distribution across different layers (subgrade, mid-base with geogrid, and base layer) at the first wheel position shows noticeable variations. For the Geogrid stiffness of 800 kN/m, the subgrade stress starts at -12.184 kN/m<sup>2</sup>, significantly drops to -66.725 kN/m<sup>2</sup> at 2m, and fluctuates, returning to -12.184 kN/m<sup>2</sup> at 10m. In the mid-base layer, the stress begins at -18.51

kN/m<sup>2</sup>, sharply decreases to -1.163 kN/m<sup>2</sup> at 2m, and decreases further to -499.725 kN/m<sup>2</sup> at 10m, reflecting substantial load redistribution through the Geogrid. The base layer stress starts at -8.148 kN/m<sup>2</sup>, peaks at 94.984 kN/m<sup>2</sup> at 4m, and stabilizes around -16.96 kN/m<sup>2</sup> at 10m, showing high localized pressure under the wheel but better stabilization overall due to the Geogrid (Figure 17 Left).

For the Geogrid stiffness of 1250 kN/m, the subgrade stress remains the same at -12.184 kN/m<sup>2</sup> at 0m, drops sharply to -66.725 kN/m<sup>2</sup> at 2m, and fluctuates similarly, returning to -12.184 kN/m<sup>2</sup> at 10m. In the mid-base layer, stress starts at -18.506 kN/m<sup>2</sup> and decreases dramatically to -1.165 kN/m<sup>2</sup> at 2m, with a significant redistribution reaching -500.21 kN/m<sup>2</sup> at 10m. The base layer stress starts at -7.691 kN/m<sup>2</sup>, peaks at 94.913 kN/m<sup>2</sup> at 4m, and drops to -16.843 kN/m<sup>2</sup> at 10m. The comparison of both Geogrid stiffnesses highlights that the 1250 kN/m Geogrid offers slightly better load redistribution, though the overall stress distribution patterns remain similar. The stress magnitudes are slightly lower in the subgrade and mid-base layers for the 1250 kN/m Geogrid, while the base layer shows similar peak stresses in both cases (Figure 17 Right).

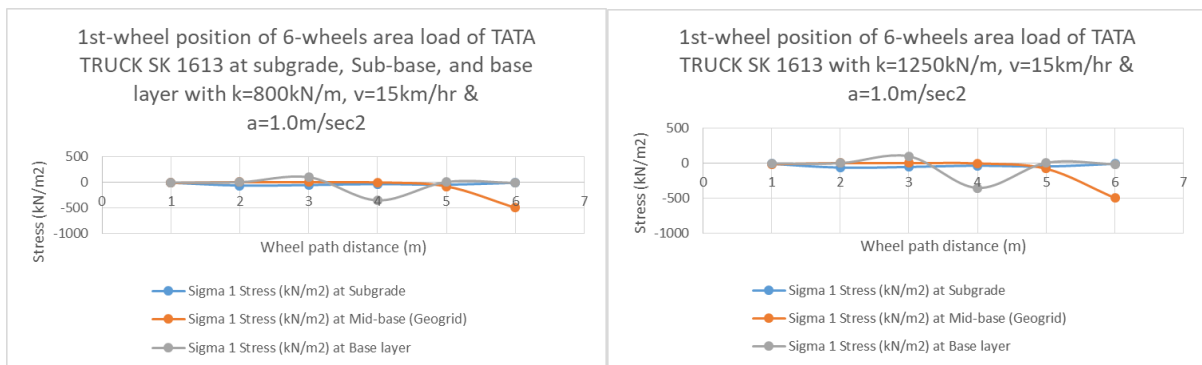


Figure 17. Sigma 1 stress distribution at the Subgrade, Mid-base, and Base layers at the first wheel position of a 6-wheel load area from a TATA TRUCK SK 1613 with  $v = 15 \text{ km/h}$ , and  $a = 1.0 \text{ m/s}^2$ : With geogrid stiffness  $k = 800 \text{ kN/m}$  (Left Figure); With geogrid stiffness  $k = 1250 \text{ kN/m}$  (Right Figure)

Figure 18 illustrates the stress distribution at the first wheel position of a 6-wheel load with geogrid reinforcement ( $k = 1250 \text{ kN/m}$ ) at a speed of  $15 \text{ km/h}$  and an acceleration of  $1.0 \text{ m/s}^2$ . In the subgrade layer, the Sigma 1 stress fluctuates significantly, ranging from  $-12.184 \text{ kN/m}^2$  at 0m to  $249077 \text{ kN/m}^2$  at 10m, indicating that stress distribution varies along the wheel path. This suggests that while the geogrid helps redistribute stress, localized variations still occur. In the mid-base layer, the geogrid reinforcement helps to reduce stress fluctuations, with the Sigma 1 stress peaking at  $-2.869 \text{ kN/m}^2$  at 4m. This shows that the geogrid enhances stress distribution, mitigating extreme stress concentrations compared to the base layer. However, in the base layer, significant peak stresses are observed at 4m, with a high Sigma 1 value of  $94.913 \text{ kN/m}^2$ . These stress concentrations indicate that while the geogrid is effective in the upper layers, the base layer still experiences substantial stress, suggesting the need for additional reinforcement to address these high stress points. Overall, geogrid reinforcement improves stress distribution in the subgrade and mid-base layers, but further efforts are needed to reduce stress concentrations in the base layer.

The results for the 4-wheel surface load with Geogrid reinforcement at  $800 \text{ kN/m}$  and  $1250 \text{ kN/m}$  stiffness (Figure 19), traveling at  $15 \text{ km/h}$  with  $1.0 \text{ m/s}^2$  acceleration, show very similar stress distributions across the subgrade, mid-base, and base layers. In the subgrade layer, the Sigma 1 stress starts at  $-9.08 \text{ kN/m}^2$  at 0m and decreases gradually to  $-6.921 \text{ kN/m}^2$  at 10m in both cases, with only minor differences between the two Geogrid stiffness values. In the mid-base layer, the stress shows a significant reduction from  $-494.273 \text{ kN/m}^2$  at 0m, but the values at 8m are almost identical, at  $-1.211 \text{ kN/m}^2$  for both stiffness values, suggesting that both Geogrid configurations perform similarly in load redistribution. In the base layer, stress fluctuates but peaks at  $-291.286 \text{ kN/m}^2$  at 6m for the  $800 \text{ kN/m}$  Geogrid and  $-265.723 \text{ kN/m}^2$  for the  $1250 \text{ kN/m}$  Geogrid, with the  $1250 \text{ kN/m}$  configuration showing slightly lower stress at 6m and more consistent stress distribution towards the end at 10m. Overall, the stress distribution is very similar for both Geogrid stiffness values, indicating that both are effective in reducing stresses, with marginal differences in their impact on the base layer stress.

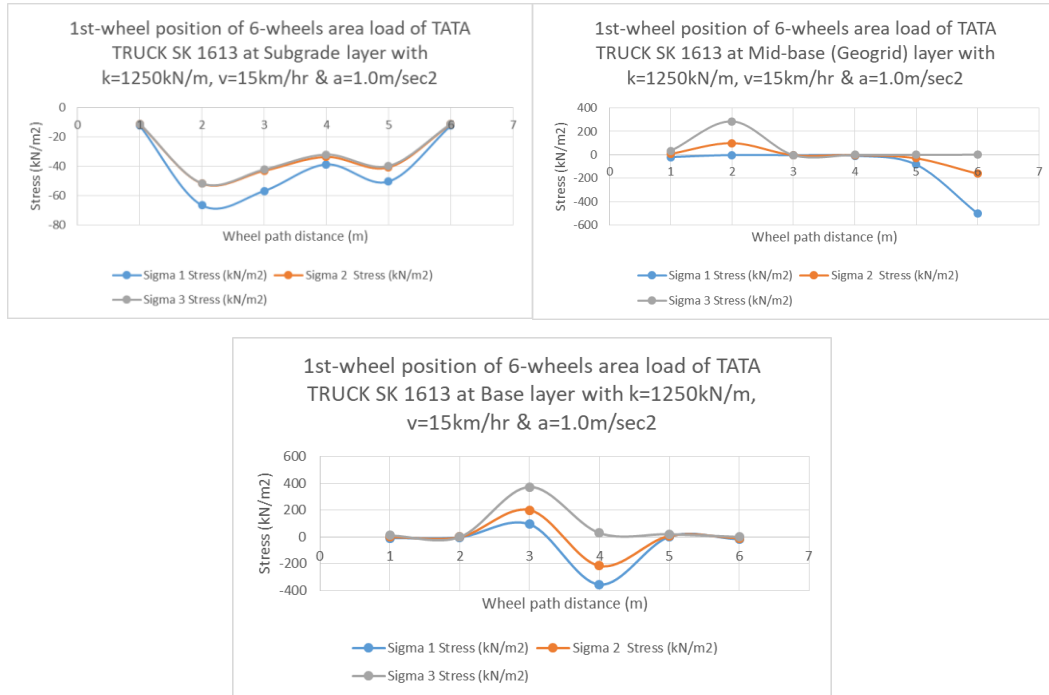


Figure 18. Sigma 1, 2, 3 stress distribution at the Subgrade, Mid-base, and Base layers at the first wheel position of a 6-wheel load area from a TATA TRUCK SK 1613, with  $k = 1250 \text{ kN/m}$ ,  $v = 15 \text{ km/h}$ , and  $a = 1.0 \text{ m/s}^2$ : Subgrade layer (Top left Figure); Mid-base layer (Top Right Figure); Base layer (Bottom Figure)

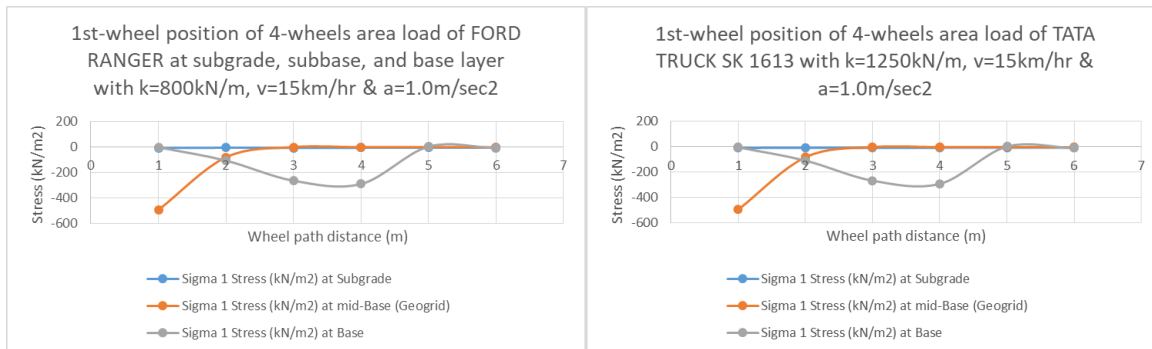


Figure 19. Sigma 1 stress distribution at the Subgrade, Mid-base, and Base layers at the first wheel position of a 4-wheel load area from a FORD RANGER, with  $k = 1250 \text{ kN/m}$ ,  $v = 15 \text{ km/h}$ , and  $a = 1.0 \text{ m/s}^2$

Figure 20 illustrates the stress distribution at the subgrade, mid-base, and base layers at the first wheel position for a 4-wheel load with Geogrid stiffness of  $1250 \text{ kN/m}$ . In the subgrade layer (top left), Sigma 1 starts at  $-9.08 \text{ kN/m}^2$  at  $0\text{m}$  and stabilizes around  $-6.92 \text{ kN/m}^2$  at  $10\text{m}$ , showing a consistent reduction in stress as the wheel moves, with minimal variation in Sigma 2 and Sigma 3. This suggests that the Geogrid does not significantly affect the subgrade stress but likely helps distribute the load across the surface. In the mid-base layer (top right), Sigma 1 stress decreases from  $-494.273 \text{ kN/m}^2$  at  $0\text{m}$  to  $-3.293 \text{ kN/m}^2$  at  $10\text{m}$ , indicating that the Geogrid is efficiently redistributing the load, particularly in the first few meters, where stress reduction is most significant. Sigma 2 shows a peak at  $56.84 \text{ kN/m}^2$  at  $10\text{m}$ , further confirming the Geogrid's role in load distribution. In the base layer (bottom middle), Sigma 1 fluctuates from  $-3.49 \text{ kN/m}^2$  at  $0\text{m}$  to a peak of  $-291.286 \text{ kN/m}^2$  at  $6\text{m}$  before decreasing again to  $-9.604 \text{ kN/m}^2$  at  $10\text{m}$ , while Sigma 3 shows large positive values at  $10\text{m}$  ( $59.581 \text{ kN/m}^2$ ). This indicates variable stress distribution, with higher fluctuations at certain points, possibly due to the combined effect of load transfer and soil-structure interaction. The Geogrid seems effective in reducing stresses in the mid-base layer but has less influence in the base layer, where variability is higher.

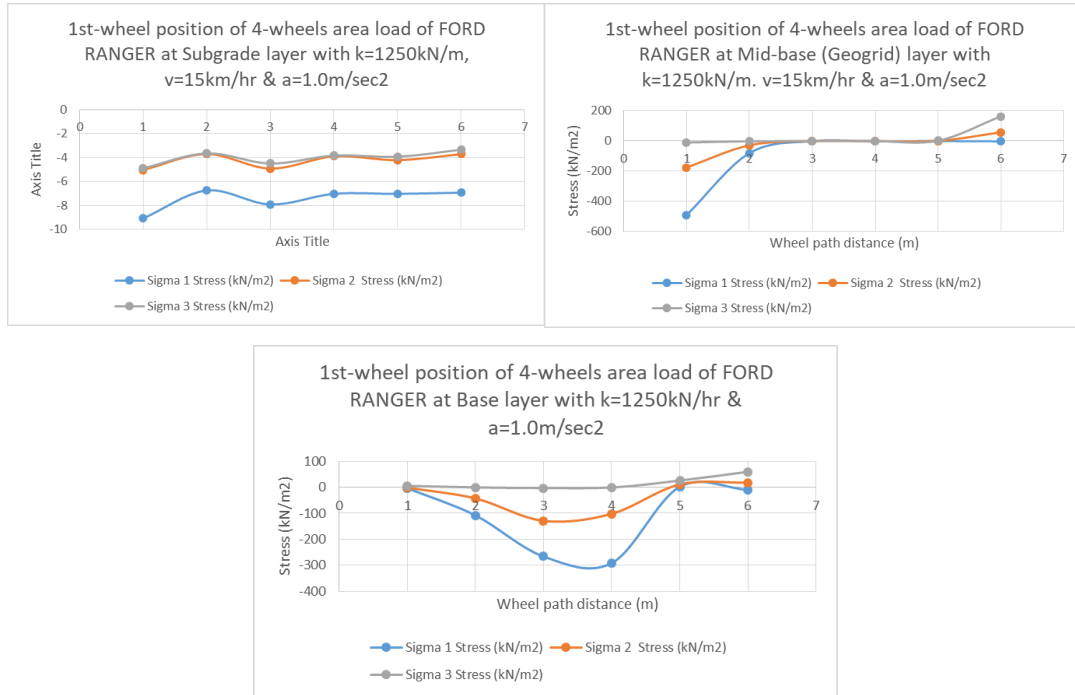


Figure 20. Sigma 1, 2, 3 stress distribution at the Subgrade, Mid-base, and Base layers at the first wheel position of a 4-wheel load area from a FORD RANGER, with  $k = 1250 \text{ kN/m}$ ,  $v = 15 \text{ km/h}$ , and  $a = 1.0 \text{ m/s}^2$ : Subgrade layer (Top left Figure); Mid-base layer (Top Right Figure); Base layer (Bottom Figure)

The 6-wheel load exhibits more pronounced variations in stress across the pavement layers compared to the 4-wheel load, particularly in the base and mid-base layers. The base layer stress shows significant fluctuations, with notable peak values observed in both load cases. The geogrid appears to redistribute the stress more effectively, especially in the mid-base and subgrade layers. However, high peak stresses still occur at certain points, especially at specific locations like the 4m position for the 6-wheel load. Overall, while the geogrid helps in redistributing stress, it does not fully eliminate substantial stress fluctuations, particularly in the deeper layers.

Figure 21 illustrates the moisture variation in a geogrid-reinforced model measured with the FORD RANGER during both dry (March 26, 2024) and wet (June 21, 2024) seasons, showing a 33% variation. The moisture content significantly impacts stress distribution and the effectiveness of geogrid reinforcement. In dry conditions, a stiffer subgrade leads to higher stress distribution, while in wet conditions, increased moisture softens the subgrade, resulting in greater stress variations, particularly in deeper layers. Given these findings, the results with drained subgrade are excluded, as undrained subgrade modeling, which accounts for fluctuating moisture, better represents the real-world conditions and is more suitable for areas with rapid moisture changes, such as seasonal climates.

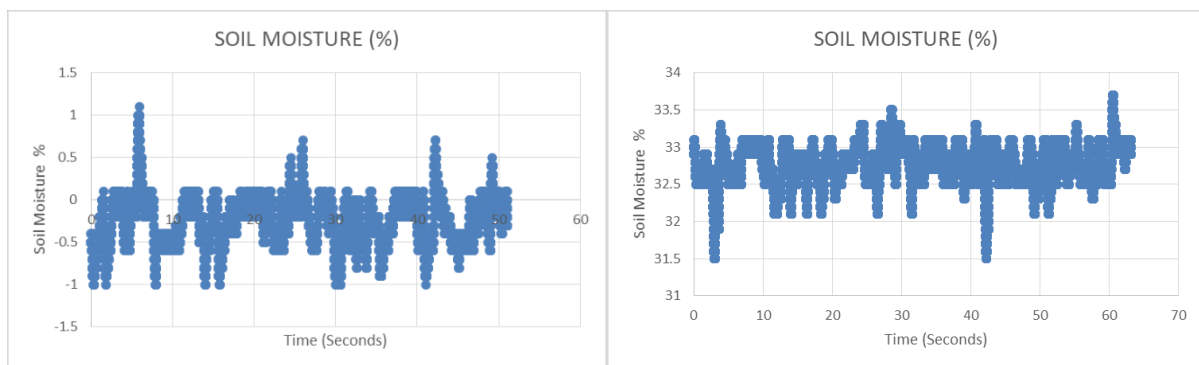


Figure 21. Moisture variation over one season measured with the FORD RANGER in the geogrid-installed model: Dry season (March 26, 2024) (Left Figure); Wet season (June 21, 2024) (Right Figure)

The significant changes in subgrade and base layer stresses, both in compression and tensile stress-strain, help mitigate structural deficiencies and surface distresses by improving stress distribution and reducing stress concentrations, thereby enhancing overall pavement performance. The enhancement in subgrade stress-strain aids in mitigating structural deficiencies, while improvements in the base layer stress-strain help alleviate surface distresses, leading to better pavement performance.

## **5. Conclusion and Recommendations**

This study examined the effectiveness of Biaxial 40/40Q Tensar geogrid ( $k = 800 \text{ kN/m}$ ) in enhancing stress distribution across pavement layers. The results indicated that the geogrid significantly reduced stress concentrations in the subgrade and mid-base layers. However, peak stresses were still observed in the base layer, especially under 6-wheel load conditions, which showed higher stress variation compared to the 4-wheel load. Seasonal moisture variations were observed to affect stress distribution, with wetter conditions causing increased stress concentrations in the subgrade due to reduced soil stiffness. Modeling the subgrade as undrained proved suitable for accurately capturing stress redistribution in regions with significant moisture fluctuation.

- **Geogrid Effectiveness:** The Biaxial 40/40Q Tensar geogrid ( $k = 800 \text{ kN/m}$ ) effectively reduces stress concentrations in the subgrade and mid-base layers, enhancing pavement performance.
- **Stress Distribution:** Stress distribution was more fluctuated under 6-wheel loading, with significant peak stresses at 4m in the base layer, indicating higher vulnerability of deeper layers under heavy traffic.
- **Moisture Influence:** A 35% variation in stress distribution was observed between dry and wet seasons, with wetter conditions causing increased stress concentrations in the subgrade due to reduced soil stiffness.
- **Undrained Subgrade Modeling:** Modeling the subgrade as undrained was more suitable for regions with significant seasonal moisture fluctuations, providing more accurate results in terms of stress redistribution.

A few recommendations can be made accordingly.

- **Optimize Geogrid Use:** Consider using higher stiffness geogrids (e.g.,  $k = 1250 \text{ kN/m}$ ) for improved performance, particularly for mitigating peak stresses in the base layer.
- **Explore Layer Configuration:** Future studies should focus on determining the optimal placement and configuration of geogrid in various pavement types and traffic load scenarios, with particular attention to deeper layers.
- **Account for Moisture Variations:** Pavement designs should incorporate seasonal moisture variations and their impact on subgrade stiffness to improve long-term stress distribution.
- **Implement Long-Term Monitoring:** Establish long-term monitoring programs to assess the performance of geogrid-reinforced pavements over time, enabling better understanding of their durability and effectiveness in various environmental conditions.

In this study, geogrid reinforcement was employed in the mid-base layer, with the assumption that fine particle migration and layer separation issues would not arise. However, if such issues do occur, it is recommended to use a composite material at the subgrade-subbase interface to prevent these problems and enhance overall pavement stability.

## **6. Acknowledgments**

We sincerely thank the Midhill Road Project team for field support, QRDC, the Department of Roads, and RTU Pulchowk for funding and monitoring assistance, CMTL and Heavy Lab staff for testing support, and Er. Hemant Tiwari, SOTEN, for his continued encouragement.

## **7. References**

- Ahirwar, M., & Mandal, A. (2017). Geogrid reinforcement in low-volume roads on weak subgrade soils. *International Journal of Pavement Engineering*, 18(5), 433-443.
- Bajracharya, M., & Sharma, S. (2015). Role of geosynthetics in improving pavement performance under dynamic loads. *Geotechnical Testing Journal*, 38(2), 121-132.

- Bhandari, N., & Bhandari, S. (2020). Numerical modeling of reinforced pavements under dynamic loads. *Transportation Geotechnics*, 23, 102273.
- Bhandari, N., & Han, J. (2010). Geogrid reinforcement for pavement design: A comparative study. *Journal of Geotechnical and Geoenvironmental Engineering*, 136(10), 1395-1403.
- Bhandari, N., & Sharbaf, H. (2019). Performance analysis of pavements with geogrid reinforcement. *Geosynthetics International*, 26(4), 370-379.
- DPR (2011). Preparation of Detailed Project Report of Puspupal (Mid-Hill) Highway Project: Final Report. Government of Nepal, Ministry of Physical Planning and Works, Planning and Design Branch, Babarmahal, Kathmandu, Nepal.
- FPDG. (2014). Flexible Pavement Design Guide. Federal Highway Administration, US Department of Transportation.
- IRC:37. (2018). Guidelines for the design of flexible pavements. Indian Roads Congress.
- Khatri, R., & Bhandari, N. (2020). Modeling geogrid-reinforced pavements under heavy traffic. *Geosynthetics International*, 27(5), 401-410.
- Khatri, R., Kumar, A., & Sharma, M. (2019). Geosynthetic-reinforced pavements for sustainable infrastructure. *Transportation Geotechnics*, 19, 78-85.
- Liu, H., Wang, H., & Wu, L. (2020). Dynamic loading effects on pavement performance: Implications for pavement design. *Journal of Transportation Engineering*, 146(1), 04019063.
- Liu, J., Wang, S., & Zornberg, J. (2019). Improvement of pavement durability using geosynthetic reinforcement. *Journal of Civil Engineering and Management*, 25(6), 512-523.
- Mandal, A., Ahirwar, M., & Roy, S. (2017). Dynamic performance of geogrid-reinforced pavements: A numerical approach. *Geosynthetics International*, 24(3), 227-237.
- Nik Daud, N., Zornberg, J., & So, C. (2019). Geosynthetic reinforcement in pavements: Applications and challenges. *Transportation Research Record*, 2673(3), 43-51.
- Pazhani, K., & Khatri, R. (2021). Pavement performance under cyclic loading: A review. *Transportation Research Part C*, 127, 102233.
- Pazhani, K., Weng, L., & Pilehvar, S. (2016). Instrumentation of geosynthetics in pavements for performance monitoring. *Geotechnical Testing Journal*, 39(2), 183-193.
- Roy, S., Bhandari, N., & Zornberg, J. (2018). Geogrid reinforcement in flexible pavements: A comparative study. *International Journal of Pavement Engineering*, 19(5), 422-433.
- Roy, S., & Sharma, P. (2019). Geogrid reinforcement in low-volume roads: A case study. *International Journal of Pavement Engineering*, 20(7), 625-637.
- Sharma, A., & Roy, N. (2021). Geogrid-reinforced pavements: Dynamic loading and performance evaluation. *Geotechnical Testing Journal*, 43(4), 5.
- Sharma, S., & Kumar, A. (2016). Geosynthetics in Pavement Design. *Transportation Geotechnics*, 9, 18-28.
- Sharma, S., Khatri, R., & Sharma, R. (2021). Dynamic performance of geogrid-reinforced pavements under heavy traffic conditions. *Geosynthetics International*, 28(4), 378-387.

- Siddique, M., Mandal, A., & Roy, S. (2020). Assessment of geogrid reinforcement in low-volume roads using numerical and physical models. *International Journal of Pavement Engineering*, 21(6), 1125-1135.
- Tang, X., Zornberg, J., & Wu, L. (2016). Performance of geosynthetic-reinforced pavements: A case study in Nepal. *Transportation Geotechnics*, 5, 50-58.
- U.S. Army Engineer Waterways Experiment Station. (1992). Correlation between California Bearing Ratio (CBR) and Dynamic Plate Load Index (DPI). Technical Report, U.S. Army Corps of Engineers, Vicksburg, MS.
- Wang, H., Liu, Y., & Wu, L. (2014). Geogrid reinforcement and its impact on pavement stability. *Journal of Geotechnical and Geoenvironmental Engineering*, 140(7), 04014033.
- Wang, L., Liu, J., & Wang, S. (2015). Impact of dynamic loading on geogrid-reinforced pavements. *Geotechnical Testing Journal*, 38(6), 594-605.
- Wu, Z., Zornberg, J., & Weng, L. (2015). Performance of geosynthetic-reinforced pavements: A comparative study. *Geosynthetics International*, 22(3), 211-220.
- Wu, Z., Zornberg, J., & Weng, L. (2020). Modeling geosynthetic-reinforced pavements under dynamic loading conditions. *Geosynthetics International*, 27(4), 344-355.
- Zhang, Y., Liu, J., & Wang, S. (2016). Geogrid-reinforced pavements: Effects of dynamic traffic loads. *Journal of Geotechnical Engineering*, 142(5), 04016001.
- Zornberg, J. (2017). Geosynthetics for sustainable pavement design. *Geosynthetics International*, 24(1), 1-15.